Theor Chem Acc (2011) 130:69–82
DOI 10.1007/s00214-011-0965-1

REGULAR ARTICLE

Microscopic binding of butyrylcholinesterase with quinazolinimine derivatives and the structure–activity correlation

Mohamed Diwan M. AbdulHameed · Junjun Liu · Yongmei Pan · Lei Fang · Carlos Silva-Rivera · Chang-Guo Zhan

Received: 28 March 2010 / Accepted: 17 May 2011 / Published online: 3 June 2011

Abstract Butyrylcholinesterase (BChE) is not only an important protein for development of anti-cocaine medication but also an established drug target to develop new treatment for Alzheimer's disease (AD). The molecular basis of interaction of a new series of quinazolinimine derivatives as BChE inhibitors has been studied by molecular docking and molecular dynamics (MD) simulations. The molecular docking and MD simulations revealed that all of these inhibitors bind with BChE in similar binding mode. Based on the similar binding mode, we have carried out three-dimensional quantitative structure–activity relationship (3D-QSAR) studies on these inhibitors using comparative molecular field analysis (CoMFA) and comparative molecular similarity indices analysis (CoMSIA), to understand the structure–activity correlation of this series of inhibitors and to develop predictive models that could be used in the design of new inhibitors of BChE. The study has resulted in satisfactory 3D-QSAR models. We have also developed ligand-based 3D-QSAR models. The contour maps obtained from the 3D-QSAR models in combination with the simulated binding structures help to better interpret the structure–activity relationship and is consistent with available experimental activity data. The satisfactory 3D-QSAR models strongly suggest that the determined BChE-inhibitor binding modes are reasonable. The identified binding modes and developed 3D-QSAR models for these BChE inhibitors are expected to be valuable for rational design of new BChE inhibitors that may be valuable in the treatment of Alzheimer's disease.

Keywords Butyrylcholinesterase · Inhibitor · Binding mode · Modeling

Electronic supplementary material The online version of this article (doi:10.1007/s00214-011-0965-1) contains supplementary material, which is available to authorized users.

M. D. M. AbdulHameed · J. Liu · Y. Pan · L. Fang · C. Silva-Rivera · C.-G. Zhan (✉)
Department of Pharmaceutical Sciences, College of Pharmacy, University of Kentucky, 789 South Limestone Street, Lexington, KY 40536, USA
e-mail: zhan@uky.edu

1 Introduction

Alzheimer disease (AD) is an irreversible, neurological disorder involving a progressive impairment of cognitive functions, accompanied by behavioral disturbances and a decreasing ability to perform basic activities of daily living [1]. It is the leading cause of dementia among older people [2]. Nearly 5 million people were reported to be affected by AD in United States [3]. The cost for treating AD is around $100 billion per year in the United States [3]. The presence of massive deposit of aggregated protein breakdown products, amyloid-β (Aβ) plaques, and neurofibrillatory tangles are characteristic neuropathology hallmark of AD [4]. Substantial loss of cholinergic activity was also reported in AD brain [2]. The decrease in cholinergic activity was reported to have correlation with the clinical dementia ratings [5]. There are very few treatment options available for AD patients. Inhibitors of cholinesterases, i.e., acetylcholinesterase (AChE) and butyrylcholinesterase (BChE), were used as treatment of choice in AD [6]. These inhibitors increase the cholinergic activity and give symptomatic relief [7]. Four of the five FDA-approved drugs for AD treatment are mainly inhibitors of AChE [8]. These currently available drugs have many side effects like liver damage, nausea, and vomiting [2, 9]. This limits the usefulness of these drugs. Hence, there is a need to

discover new compounds that could be developed as drugs for AD treatment. More recent studies have shown that BChE is a promising target for the treatment of AD. BChE is a well-known enzyme used for various therapeutic purposes, including anti-cocaine medication [10]. BChE is synthesized in liver and widely distributed in the body, including plasma, brain, and lung [11, 12]. But its physiological function has not completely been elucidated. There is growing evidence that BChE is involved in the development and progression of AD. Over expression of BChE was reported in neuritic Aβ plaques in the AD brain [13]. BChE not only hydrolyzes butyrylcholine but also inactivates acetylcholine. The key role of BChE to compensate the role of AChE is shown by the survival of AChE knockout mice with normal levels of BChE [14]. Recent report has revealed that in advanced AD, the AChE level decreases whereas the BChE level increases [15]. BChE is also reported to have a possible role in the aggregation of β-amyloid protein (Aβ) [8]. Individuals without BChE activity due to a genetic variation were reported to be healthy and no physiological abnormality was reported [16, 17]. This shows that inhibition of BChE can be achieved without severe side effects. Selective BChE inhibitors were reported to elevate extracellular acetylcholine levels [15]. Selective BChE inhibitors were also reported to improve the cognitive performance of aged rats [15]. Developing BChE inhibitor will have potential therapeutic benefits in AD treatment.

A series of quinazolinimine derivatives were reported as BChE inhibitors by Decker et al. [18–20] Understanding how BChE binds with these inhibitors, exploring their structure–activity relationship (SAR), and developing predictive computational models will be valuable in rational design of more potent inhibitors. Computational drug design studies were reported to be successful in such lead optimization studies [21]. Understanding the detailed BChE-inhibitor binding structures is clearly valuable for structure-based drug design, where the detailed 3D structure of the drug target (receptor) is used and molecular docking is performed to determine the binding mode of the target protein with each possible drug candidate [22, 23]. Besides, 3D-quantitative structure–activity relationship (3D-QSAR) is a ligand-based drug design method which is widely used in lead optimization studies [24]. 3D-QSAR methods serve as an important complement to structure-based methods [24]. The main goal of the 3D-QSAR modeling is to develop a statistically significant and highly predictive model. Such a model is then used to predict the activity of new compounds to be synthesized. Comparative molecular field analysis (CoMFA) and comparative molecular similarity indices analysis (CoMSIA) are the two 3D-QSAR methods which have been successfully employed in new drug design [25–28]. Such approaches were useful in the lead optimization and help us to understand the receptor-ligand interaction [29–31]. In CoMFA, the biological activity of molecules is correlated with their steric and electrostatic energies [32]. The steric and electrostatic interaction energies are calculated using Lennard-Jones potential and Coulombic potential, respectively [25]. In CoMSIA, similarity indices are calculated at regularly placed grid points for the aligned molecules [28]. CoMSIA includes additional molecular descriptors like hydrophobic fields and hydrogen bond donor and acceptor fields [28]. The contour maps were obtained as a graphical output from these methods, and it highlights the regions in space where the aligned molecules can favorably or unfavorably interact with a possible environment [7]. These contour maps can also be used to get an insight into the topological features in receptor site [31]. Our most recent study indicates that receptor-based (or docking-based) 3D-QSAR methods also give good results in lead optimization [33]. In this method, the docked molecules were used as a starting point to carry out 3D-QSAR analysis rather than aligning the ligand using a low-energy conformer template.

In the present study, we mainly aimed to understand how BChE binds with this important series of inhibitors, i.e., quinazolinimine derivatives, and determine the detailed binding structures. The detailed 3D structures of BChE binding with a total of 42 inhibitors have been determined by molecular docking followed by molecular dynamics simulations. To examine whether the docked BChE-inhibitor binding structures are reasonable or not, we have also carried out various 3D-QSAR analyses on these inhibitors by using both CoMFA and CoMSIA methods. All of the obtained ligand-based and receptor-based CoMFA and CoMSIA models and the corresponding contour maps strongly support the docked BChE-inhibitor binding structures. As a byproduct of the current study, the obtained 3D-QSAR models are capable of predicting the inhibitory activity of the BChE inhibitors. The determined BChE-inhibitor binding modes and the developed 3D-QSAR models are expected to be valuable in future rational design of more potent inhibitors of BChE.

2 Computational details

2.1 Data sets

All compounds used in the present study were reported recently by Decker et al. as inhibitors of BChE [18–20]. The IC_{50} values were converted into pIC_{50} (i.e., $-\log IC_{50}$) values for the 3D-QSAR studies. The structures of the compounds and their pIC_{50} values are given in Table 1.

Table 1 Molecular structures of compounds used in the training- and test sets and their BChE inhibitory activity

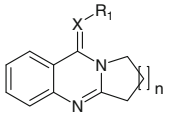

Compd.	X	R_1	n	BChE IC_{50} (μM)	pIC_{50}
1	N		1	19.5	4.71
2[a]	N		2	22.3	4.65
3	N		3	4.1	5.39
4	N		4	2.3	5.64
5	N		1	1.87	5.73
6	N		2	1.4	5.85
7	N		3	1.5	5.82
8[a]	N		4	1.1	5.96
9	N		1	0.62	6.21
10	N		2	0.144	6.84
11	N		3	2.2	5.66
12	N		4	0.62	6.21

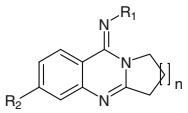

Compd.	R_1	R_2	n	BChE IC_{50} (μM)	pIC_{50}
14	H	H	1	7.2	5.14
15	H	H	4	3.0	5.52
16	$COCH_3$	H	1	204.0	3.69
17	C_4H_9	Cl	1	2.3	5.64
18	C_4H_9	H	1	5.5	5.26

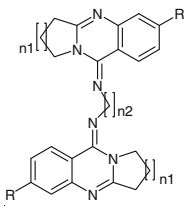

2.2 Molecular docking

Molecular docking was carried out to understand the detailed binding modes of BChE binding with these inhibitors. The X-ray crystal structure (PDB ID: 1P0M) of BChE was used in molecular docking. The 3D structures of all compounds were built using the SYBYL software (Tripos, Inc.). The geometries of all compounds were optimized by using semiempirical PM3 method. The optimized geometries were used to perform single-point

Table 1 continued

Compd	R	n1	n2	BChE IC_{50} (μM)	pIC_{50}
19	Cl	1	7	0.061	7.21
20[a]	H	1	7	0.088	7.06
21	H	2	7	0.0085	8.07
22	H	3	7	0.024	7.62
23	H	4	7	0.027	7.57
24	Cl	1	8	0.0454	7.34
25	H	1	8	0.0048	8.32
26	H	2	8	0.0076	8.12
27	H	3	8	0.013	7.89
28	H	4	8	0.076	7.12

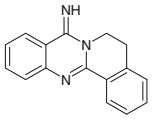

13. BChE IC_{50} = 2.0μM (pIC_{50} = 5.67)

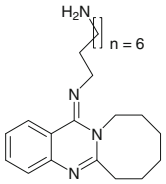

35. BChE IC_{50} = 0.046μM (pIC_{50} = 7.34)

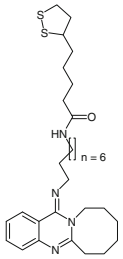

42. BChE IC_{50} = 0.023μM (pIC_{50} = 7.64)

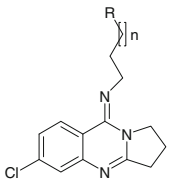

Compd	R	n1	BChE IC_{50} (μM)	pIC_{50}
29	NH_2	1	10.23	4.99
30[a]	NH_2	2	0.72	6.14
31	NH_2	3	0.19	6.72
32	NH_2	4	0.38	6.42
33	NH_2	5	0.71	6.15
34	NH_2	6	0.012	7.92
36	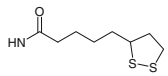	1	2.58	5.59
37	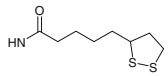	2	0.17	6.77
38	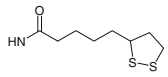	3	0.053	7.28
39	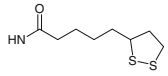	4	0.026	7.59
40	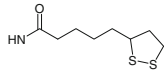	5	0.014	7.85
41[a]	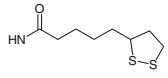	6	0.0057	8.24

pIC_{50} values calculated from the IC_{50} data in Refs. [18–20]

[a] Compounds used in the test set were based on random selection

ab initio calculations at the HF/6-31G* level in order to determine the electrostatic potential (ESP)-fitted atomic charges, i.e., the ESP charges, that fit to the electrostatic potential at points selected according to the Merz-Singh-Kollman scheme [34, 35]. Molecular docking was carried out by using FlexX module of SYBYL [36]. The FlexX uses incremental docking algorithm called pose clustering [36]. In this program, the ligand molecule is split up into fragments and the core fragment is first placed according to the given scoring function [37]. The molecule is built up by performing conformational search of the ligand in the active site [36]. Only the best conformation was built upon and the others are discarded. The active site was defined as residues within 9.5 Å around the bound choline molecule, Thr120, Val288, and Tyr332. The active site is defined such that the entire active-site cavity is covered in docking. Based on the crystal structure, the region with residues Trp82, His438, and Ser198 were defined as the core sub-pocket. The ligands were docked using the multiple-ligand docking option of FlexX. The top-75 docked orientations were generated for each ligand. The best docked structure was selected based on the FlexX score and visual checking of the docked pose.

2.3 Molecular dynamics simulation

The general procedure used to carry out the MD simulations in this study is essentially the same as that used in our earlier computational studies [38]. Briefly, the MD simulations were performed using Sander module of Amber8 program [39]. The force field parameters used for ligands were determined by using the standard general amber force field (GAFF) associated with the Antechamber module of the Amber8 program. The BChE-ligand binding complex was neutralized by adding appropriate counter ions and was solvated in a rectangular box of TIP3P water molecules [40] with a minimum solute-wall distance of 10 Å. The solvated systems were carefully equilibrated and fully energy-minimized. These systems were gradually heated from $T = 10$ K to $T = 298.15$ K in 35 ps before a production MD simulation run. The time step used for the MD simulations was 2 fs. Periodic boundary conditions in the NPT ensemble at $T = 298.15$ K with Berendsen temperature coupling [41] and $P = 1$ atm with isotropic molecule-based scaling were applied. The SHAKE algorithm was used to fix all covalent bonds containing hydrogen atoms [42]. The particle mesh Ewald (PME) method [43] was used to treat long-range electrostatic interactions. Restrain was placed on the C-alpha backbone atoms during the MD run. A residue-based cutoff of 12 Å was utilized to the non-covalent interactions. Production MD was then carried out for 1 ns or more with 2 fs time step. The time-dependent geometric parameters were carefully examined to make sure that we obtained a stable MD trajectory for each simulated protein–ligand binding system. The coordinates of the simulated system were collected every 1 ps during the simulation.

2.4 3D-QSAR analysis

Of the 42 compounds reported, 37 compounds were used as a training set and the remaining five compounds were used as a test set, based on a random selection. The compounds in the test set have a range of biological activity values similar to that of the training set. The pIC_{50} values of the compounds studied cover an interval of more than 3 log units.

The pose obtained from the MD simulation was used as a starting point for the 3D-QSAR study. The CoMFA and CoMSIA models were generated by using the SYBYL software with the default parameters. A regularly placed grid of 2.0 Å was created around the molecules obtained from MD simulations. The 3D-QSAR model was generated by considering the entire ligand structure without ignoring any particular ligand region. The generated grid completely covered the docked molecules. In CoMFA, the steric and electrostatic fields were calculated at each intersection lattice point of the grid. A sp^3 carbon atom with charge +1.00 was used as a probe atom. The steric and electrostatic fields were truncated at +30.0 kcal/mol. In CoMFA, the standard scaling applies equal weight to all lattice points in a given field. The region focusing option helps to refine the CoMFA model. It increases the weight to those lattice points which are important for the model [44]. We used region focusing to develop the CoMFA models in this study. In CoMSIA, the steric, electrostatic, hydrophobic, hydrogen bond donor and acceptor descriptors were calculated at each lattice intersection of a regularly placed grid of 2.0 Å. A probe atom with radius 1.0 Å, charge +1.0, and hydrophobicity of +1.0 was used to calculate the respective fields. The attenuation factor α was set to 0.3.

The partial least-square (PLS) analysis was used to derive the 3D-QSAR models. Sample-distance PLS (SAMPLS) algorithm [45] was used for the leave-one-out (LOO) cross-validation. The optimum number of the components identified in the cross-validation was used in the final analysis. To further validate the model, 100 runs of bootstrap analyses were performed. The models were also rigorously analyzed by performing cross-validation using five groups and two groups in the training set. Since only the number of groups and the number of validation times can be controlled in the SYBYL "cross-validation" process, the process was repeated for 25 times. The models were also evaluated for their ability to predict the activity of molecules in the test set. The predictive r^2 (denoted by r^2_{pred}) for molecules in the test set was calculated by using Eq. (1):

$$r^2_{\text{pred}} = (\text{SD} - \text{PRESS})/\text{SD} \quad (1)$$

where SD is the sum of the squared deviations of the individual biological activity values for the test-set molecules from the mean activity value of the test-set molecules and PRESS is the sum of the squared deviations of the predicted activity values from the actual activity values of the test-set molecules. Contour maps were generated as the output of these 3D-QSAR models. The contour maps generated depict regions having scaled coefficients greater than 80% (favored) or less than 20% (disfavored).

The quantum mechanical (QM) calculations using Gaussian03 were performed on an IBM X-series cluster with 340 nodes and 1,360 processors at University of Kentucky Center for Computational Sciences. The 3D-QSAR analyses and FlexX docking were performed by using SYBYL 7.0 software [46] on a Silicon Graphics Fuel workstation and the other computations were carried out on a 34-processors IBM ×335 Linux cluster in our own laboratory.

3 Results and discussion

3.1 Microscopic binding modes from molecular docking and molecular dynamics simulations

Molecular docking followed by molecular dynamics (MD) simulations was carried out for all of the 42 inhibitors in order to understand the nature of the interactions of these compounds with BChE. The overall crystal structure of *human* BChE along with the active-site cavity is provided as supporting information (Figure S1). BChE has a 20 Å deep gorge that leads to the active site penetrating half way into the enzyme, and it is 5 Å wider [11]. The key features in the BChE active-site gorges are the (1) catalytic triad (Ser198, Glu325, and His438), (2) the oxyanion hole (Gly116, Gly117, and Ala199), (3) the acyl pocket (Val288, Leu286, and Phe329), and (4) the choline-binding pocket formed from residues including Trp82. The difference between the active-site gorges of BChE and the related AChE is that a few aromatic residues lining the gorge of AChE are replaced with smaller hydrophobic residues in BChE [47]. For example, two of the acyl pocket residues Phe290 and Phe288 in *Tc*AChE are mutated to smaller residues Val288 and Leu286 in BChE.

The docked poses of all 42 compounds in BChE active site is shown in Fig. 1. The different regions in this ligand series used to describe SAR are marked in Fig. 2. The docking was followed by 1–2 ns MD simulation for inhibitor. The pose obtained from the MD simulation was taken for final analysis. For each compound, the MD simulation eventually led to a stable MD trajectory, demonstrating that

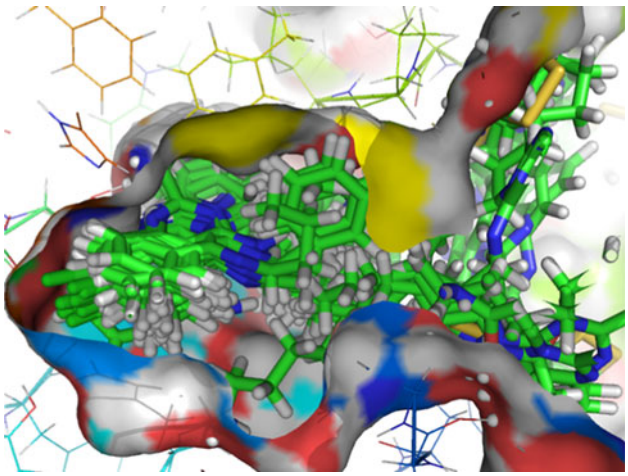

Fig. 1 Spliced view of BChE active-site cavity with 42 docked inhibitors

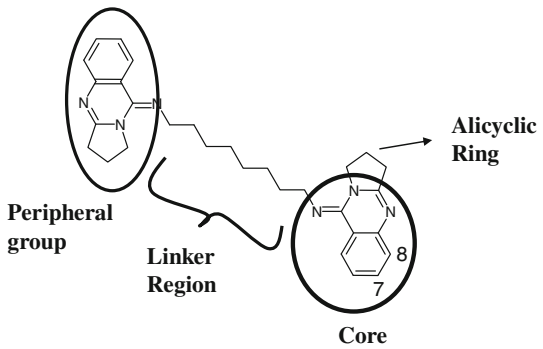

Fig. 2 Compound **25** is shown along with labels used in the discussion of SAR for this ligand series reported in Refs. [18–20]

the final binding structure obtained from the MD simulation is stable. As representative examples, the MD trajectories and the binding structures obtained for the compounds **25** and **41** were depicted in Figs. 3, 4, 5, 6. In particular, concerning the stability of the MD trajectory depicted in Fig. 3, we also continued the MD simulation until 4 ns (see Figure S6 in supporting information) and confirmed that the MD-simulated binding structure is stable. Further, we carefully compared the MD-simulated binding structure with the binding structure obtained from the initial docking and found no significant difference in the BChE active-site structure, suggesting that the BChE active-site structure is relatively rigid. In addition, we also examined possible participation of solvent in the binding and found no solvent water molecule involved in the binding.

The binding mode of the most active compounds, i.e., compounds **25** and **41,** are described as the representatives of this series. The binding mode of the most active compound in this series, i.e., compound **25**, with BChE is shown in Fig. 4. Binding mode of compound **25** shows that

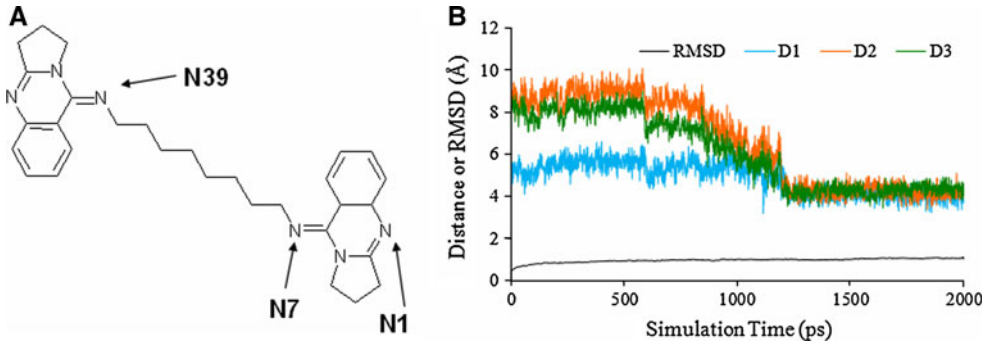

Fig. 3 **a** Molecular structure of compound **25**. **b** Plots of MD-simulated internuclear distances versus simulation time for BChE binding with compound **25**. *D1* refers to the distance between N7 atom of compound **25** and the carbonyl oxygen of Gly116 backbone, *D2* the distance between N39 atom of compound **25** and the OG atom of Ser287 side chain, and *D3* the distance between N39 atom of compound **25** and the N atom of Thr284 backbone

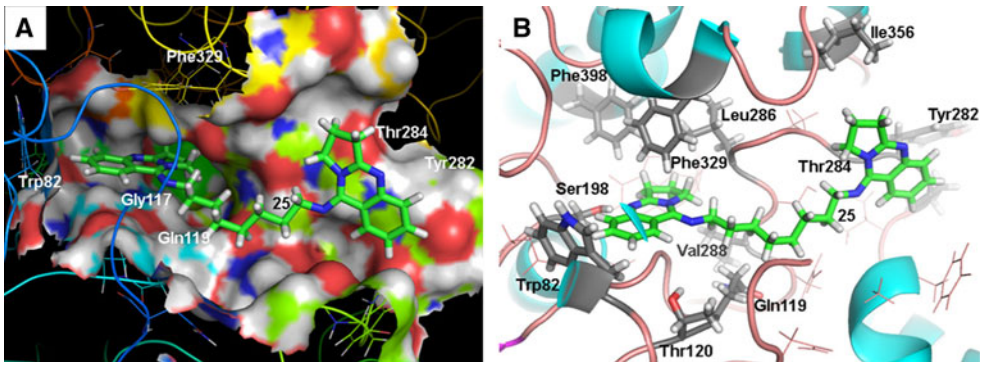

Fig. 4 Binding mode of compound **25** with BChE active site. Compound **25** is shown in sticks with carbon atoms in *green color*. Important residues involved in binding are *marked*. **a** BChE active site shown as *solid* surface. **b** BChE active site shown as *cartoon*. Residues interacting with compound **25** are highlighted in *gray color*

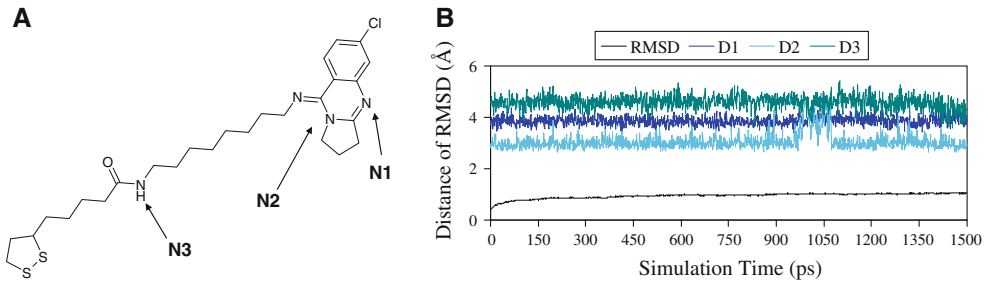

Fig. 5 **a** Molecular structure of compound **41**. **b** Plots of MD-simulated internuclear distances versus simulation time for BChE binding with compound **41**. *D1* refers to the distance between N2 atom of compound **41** and the NH nitrogen of Gly114 backbone, *D2* the distance between N3 atom of compound **41** and the carbonyl oxygen of Ile66 backbone, and *D3* the distance between N1 atom of compound **41** and the NE2 atom of His435 side chain

the residues Gly116 and Gly117 lie below the plane of quinazolinimine group in the core region. It forms the base for the binding of quinazolinimine group. The ligand core group is surrounded by hydrophobic residues. The hydrophobic residue Phe329 lies perpendicularly to the plane of quinazolinimine group in the core region. Trp82 and Ile442 are present on one side of the quinazolinimine group. The five-membered ring attached to quinazolinimine group is present in a hydrophobic cavity and is surrounded by residues Trp231, Leu286, Val288, Phe329, Phe398, and Ala199. Ser198 and His438 are present near to nitrogen atom of the quinazolinimine core group. The octa-methylene linker group interacts with the side chain methyl group of Thr120 and the side chain $-(CH_2)_2-$ group of Gln119. The quinazolinimine group in the peripheral region favorably interacts with the backbone –CO–NH– groups of

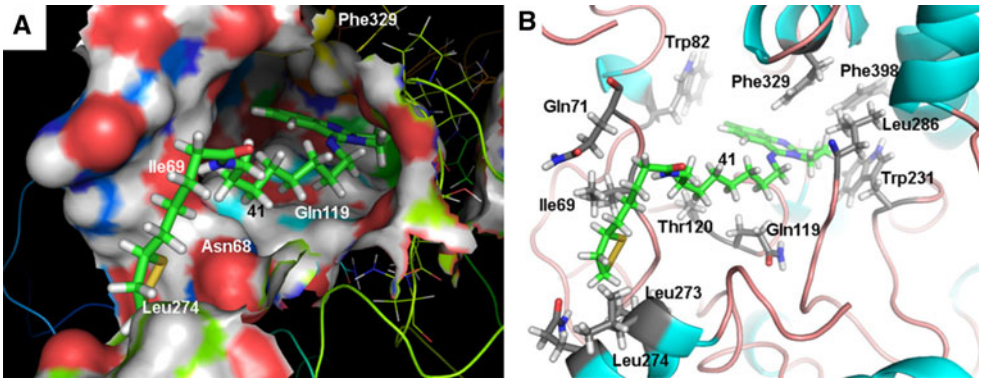

Fig. 6 Binding mode of compound **41** with BChE active site. Compound **41** is shown in *sticks* with carbon atoms in *green color*. Important residues involved in binding are *marked*. **a** BChE active site shown as *solid* surface. **b** BChE active site shown as *cartoon*. Residues interacting with compound **41** are highlighted in *gray color*

Tyr282, Gly283, and Thr284. An inspection of the detailed binding structures reveals that the five-membered alicylic ring attached to the quinazolinimine group is optimal for binding in BChE pocket. This is in agreement with the reported SAR which shows that compounds **26–28** have a slightly lower activity than compound **25**.

The binding mode of the second most active compound in this series, i.e., compound **41**, is shown in Fig. 6. In the case of compound **41**, quinazolinimine group in the core region binds in a similar orientation as compound **25**. The five-membered ring attached to quinazolinimine group is surrounded by hydrophobic residues Trp231, Leu286, Val288, Phe329, Phe398, and Ala199. Gly116 and Gly117 lie below and Phe329 lies above the plane of quinazolinimine group in the core region. The octa-methylene linker group interacts with the side chain methyl group of Thr120, the side chain $–(CH_2)_2–$ group of Gln119 and the side chain $–CH_2$ group of Asn68. This linker group helps to position the lipoic acid group at the entrance of the active site. Our docking shows that altering the linker length changes the orientation of lipoic acid group. As can be seen from the data for compounds **36–41**, the increase in the chain length of the linker region increases the activity of the compound. The octa-methylene linker is the optimal chain length and orients the lipoic acid group toward a cavity at the entrance surrounded by hydrophobic residues Ile69, Leu273, and Leu274. The hydrophobic chain of lipoic acid has favorable hydrophobic interaction with the Ile69 and the $–(CH_2)_2–$ side chain of Gln71. The amide group connecting the lipoic acid with the octa-methylene linker group in compound **41** forms a hydrogen bond with the backbone carbonyl group of residue Ile69. Lipoic acid group also interacts with residues Leu273, Leu274, and Gln270 on one side. Compound **16** has the lowest activity in this series. Figure S3 in supporting information shows the MD trajectories for compounds **16**. The binding mode of compound **16** with BChE is provided in supporting information (Figure S4). In the case of compound **16**, quinazolinimine group in the core region binds with BChE in a similar orientation as other compounds in this series. Phe329 lies above the plane of quinazolinimine group. The five-membered ring attached to quinazolinimine group is surrounded by hydrophobic residues Trp231 and Leu286. Compound **16** has a carbonyl group attached directly to the imine nitrogen (Figure S4 in supporting information). Our docking and MD-simulated structures reveal that this carbonyl group is not favored at this position and, thus, contributes to the lower activity of this compound. The carbonyl group of compound **16** is oriented toward the backbone carbonyl group of Gly116 (Figure S4 in supporting information) and will have unfavorable electrostatic interaction. This explains the lower activity of this compound. The results from our docking study are in agreement with the observed SAR for this series of ligands. Moreover, the docked poses also serve as a very good starting point for carrying out receptor-based 3D-QSAR modeling.

3.2 3D-QSAR models

3D-QSAR is a ligand-based approach but can be used to complement the structure-based approach like docking. In general, 3D-QSAR methods give contour plots as output. These contour plots provide some useful insight into the nature of the binding in the active site. So we also used 3D-QSAR to analyze whether the obtained 3D-QSAR models support our determined binding modes from molecular docking and MD simulations. The results from the CoMFA and CoMSIA models using the training set of 37 compounds were summarized in Table 2. In general, for all the 3D-QSAR models, a leave-one-out (LOO) cross-validation was done first to identify the cross-validated correlation coefficient (q^2) values. Then the number of components identified in the LOO cross-validation process was used in the final non-cross-validated PLS run. The developed 3D-QSAR models were analyzed in terms of various statistical parameters, namely cross-validated correlation coefficient (q^2), non-cross-validated correlation coefficient (r^2), standard error estimate (SEE), and F-statistic values. A q^2 value of greater than 0.5 is usually considered significant

Table 2 Summary of the results obtained from the CoMFA and CoMSIA analyses

PLS statistic	Model with training set of 37 compounds					Model with training set of 42 compounds				
	CoMFA 1a SE	CoMSIA 1b SE	CoMSIA 1c SEH	CoMSIA 1d SEHD	CoMSIA 1e SEHDA	CoMFA 2a SE	CoMSIA 2b SE	CoMSIA 2c SEH	CoMSIA 2d SEHD	CoMSIA 2e SEHDA
Q^2	0.732	0.726	0.696	0.75	0.75	0.793	0.75	0.723	0.781	0.786
SEP	0.656	0.643	0.646	0.669	0.645	0.573	0.611	0.619	0.589	0.591
r^2	0.974	0.950	0.850	0.981	0.973	0.970	0.943	0.849	0.967	0.969
SEE	0.204	0.273	0.454	0.186	0.211	0.219	0.293	0.456	0.229	0.226
F value	155.407	118.963	96.243	132.653	126.878	155.493	118.407	109.879	141.796	127.206
NOC	7	5	2	10	8	7	5	2	7	8
r^2_{pred}	0.825	0.728	0.862	0.796	0.824	–	–	–	–	–
r^{2a}_{bs}	0.986	–	–	–	0.981	–	–	–	–	–
Fraction										
Steric	0.457	0.346	0.333	0.185	0.165	0.479	0.368	0.334	0.189	0.168
Electrostatic	0.543	0.654	0.338	0.352	0.269	0.521	0.632	0.325	0.320	0.257
Hydrophobic	–	–	0.329	0.243	0.211	–	–	0.340	0.228	0.209
Donor	–	–	–	0.220	0.235	–	–	–	0.263	0.248
Acceptor	–	–	–	–	0.119	–	–	–	–	0.118

CoMFA and CoMSIA models were developed using common substructure-based alignment; *S* steric, *E* electrostatic, *H* hydrophobic, and *A* acceptor

[a] 100 runs of bootstrap analysis

[48]. All 3D-QSAR models developed have a q^2 value greater than 0.5. We developed ligand-based and receptor-based 3D-QSAR models. In ligand-based 3D-QSAR, substructure-based alignment of compounds was carried out (see supporting information). In ligand-based 3D-QSAR, we developed two types of models. First, we developed a model using a training set of 37 compounds. The predictive ability of the models was validated using the external test set of five compounds. These five compounds were not used in initial model development. Our second model was developed using all the 42 molecules as the training test as this will allow us to utilize all the available information.

The CoMFA models were developed after PLS region focusing. The best CoMFA model (see Table 2) using a training set of 37 molecules has a q^2 value of 0.732 and an r^2 value of 0.974. The CoMSIA model with steric, electrostatic, hydrophobic, donor, and acceptor descriptors was associated with larger q^2 and r^2 values. Hence, the CoMSIA model (denoted by CoMSIA-1e) from alignment I was selected for final analysis based on the larger r^2_{pred} value and used to predict the activity of the compounds (see Table 2). The CoMSIA-1e model has a q^2 value of 0.75 and an r^2 value of 0.973. The models have larger r^2, q^2, and F values. These data suggest that the models are reasonable for the predictive ability. The CoMFA-1a model shows that the electrostatic part plays a major role. The CoMSIA-1e model shows that electrostatics play major role followed by hydrophobic contribution. The hydrogen bond acceptor is found to have the least contribution to the activity. The 3D-QSAR models were further validated using an external test set of five compounds. CoMFA-1a and CoMSIA-1e models all gave good predictions of both the training- and test-set compounds (see supporting information). Both the CoMFA-1a and the CoMSIA-1e models have sufficiently large r^2_{pred} values, i.e., 0.825 and 0.824, respectively. The predicted activity of the compounds and their residuals (deviations) are given in supporting information and the plots obtained were depicted in Fig. 7a and b. In both models (CoMFA-1a and CoMSIA-1e), the deviations of the predicted pIC_{50} values from the corresponding experimental pIC_{50} values are always smaller than 1 log unit. The CoMFA-1a and CoMSIA-1e models were further analyzed by additional rigorous statistical cross-validation using five and two groups in the training set. Each cross-validation process was repeated for 25 times, and the results are given in supporting information (Table S5). As shown in Table S5, the average q^2 values obtained in this way were only slightly lower than the q^2 values obtained with the LOO method. These results suggest that the high q^2 values were not obtained by chance correlation and the obtained CoMFA-1a and CoMSIA-1e models are stable and valid. We also carried out 100-run of bootstrap analyses and both models have high value of boot-strap r^2 (see Table 2). The final 3D-QSAR models (CoMFA-2a and CoMSIA-2e) were developed using all the 42 compounds as the training set. Contour plots generated using this model was used in

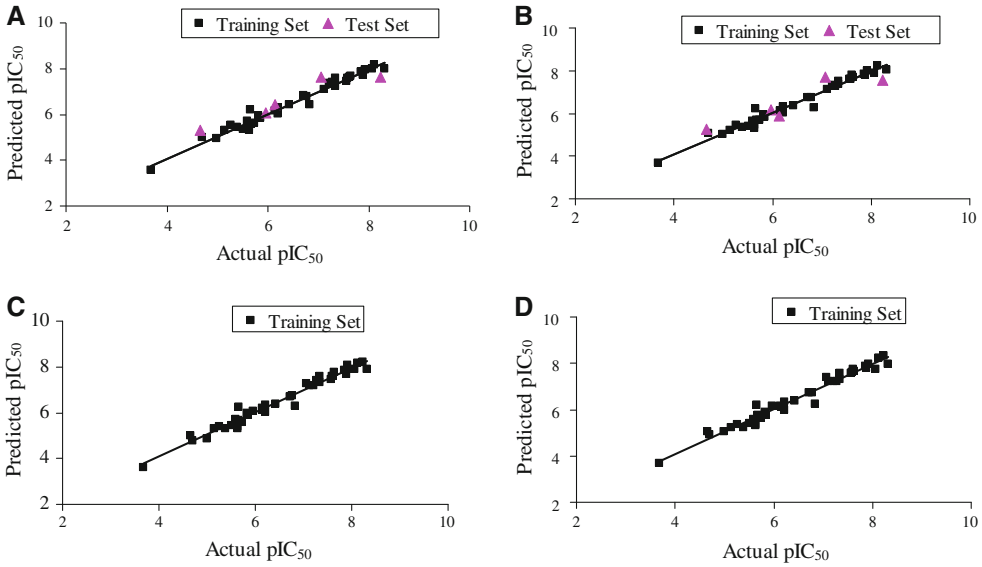

Fig. 7 Plots of the predicted pIC_{50} values versus the actual pIC_{50} values. **a** CoMFA-1a model using the training set of 37 compounds; **b** CoMSIA-1e model using the training set of 37 compounds; **c** CoMFA-2a model using the training set of 42 compounds; **d** CoMSIA-2e model using the training set of 42 compounds

our final analyses of ligand-based 3D-QSAR models. Figure 7c and d give the graph of predicted versus actual pIC_{50} value for CoMFA-2a and CoMSIA-2e, respectively. In both CoMFA-2a and CoMSIA-2e models, the deviations of the predicted pIC_{50} values from the corresponding experimental pIC_{50} values are always smaller than 1 log unit.

In addition to the ligand-based 3D-QSAR, we have also performed receptor-based 3D-QSAR analysis. The docked poses of the 42 compounds in the BChE active site were used to develop receptor-based 3D-QSAR models. The results of receptor-based 3D-QSAR are summarized in Table 3. The predictive ability of these models was also tested by using 5 compounds as an external test set. Final CoMFA and CoMSIA models were developed using all the 42 compounds as the training set. The contour plots from CoMFA-4a and CoMSIA-4b were used in the final analysis.

3.3 3D-QSAR contour maps

One of the attractive features of the CoMFA and CoMSIA modeling is the visualization of the results as 3D-coefficient contour plots. In the case of CoMFA, the green contour shows favorable steric interaction and the yellow contours show the region where steric group is not favored.

Table 3 Results obtained from the receptor-based CoMFA and CoMSIA analyses

PLS statistic	Model with training set of 37 compounds					Model with training set of 42 compounds				
	CoMFA 3a SE	CoMSIA 3b SE	CoMSIA 3c SEH	CoMSIA 3d SEHD	CoMSIA 3e SEHDA	CoMFA 4a SE	CoMSIA 4b SE	CoMSIA 4c SEH	CoMSIA 4d SEHD	CoMSIA 4e SEHDA
q^2	0.579	0.551	0.532	0.514	0.539	0.595	0.604	0.54	0.531	0.52
SEP	0.795	0.835	0.868	0.899	0.877	0.789	0.792	0.797	0.862	0.898
r^2	0.987	0.996	0.99	0.998	0.998	0.996	0.995	0.878	0.996	0.99
SEE	0.138	0.079	0.046	0.056	0.050	0.083	0.088	0.411	0.082	0.043
F value	486.14	1,245.97	3,169.75	1,841.11	2,304.74	1,307.87	994.4	104.02	1145.3	3,202.5
NOC	5	6	7	8	8	6	7	2	7	9
Fraction										
Steric	53	41	28	22	16	52	40	32	21	16
Electrostatic	47	59	43	32	25	48	60	35	32	26
Hydrophobic	–	–	29	24	19	–	–	33	24	19
Donor	–	–	–	22	21	–	–	–	23	20
Acceptor	–	–	–	–	19	–	–	–	–	19

CoMFA and CoMSIA models were developed using the alignment based on the docked poses; *S* steric, *E* electrostatic, *H* hydrophobic, *D* donor, and *A* acceptor

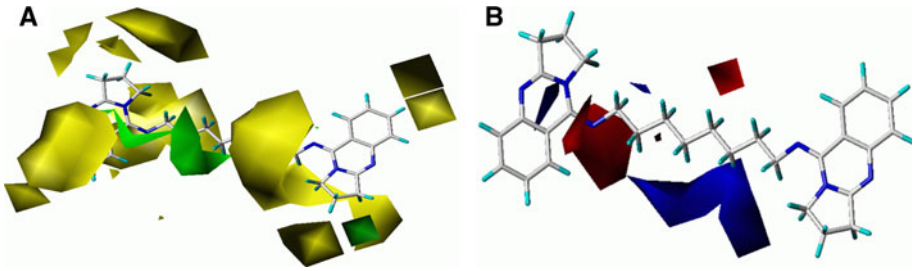

Fig. 8 **a** CoMFA steric contour maps around compound **25** and **b** CoMFA electrostatic contour maps around compound **25**. *Green* isopleths enclose areas where steric interaction is favored. *Yellow* contours are areas where the steric interaction is disfavored. *Blue* region represents the area where electropositive group is favorable for the binding. *Red* region refers to the area where an electronegative group is favorable for the binding

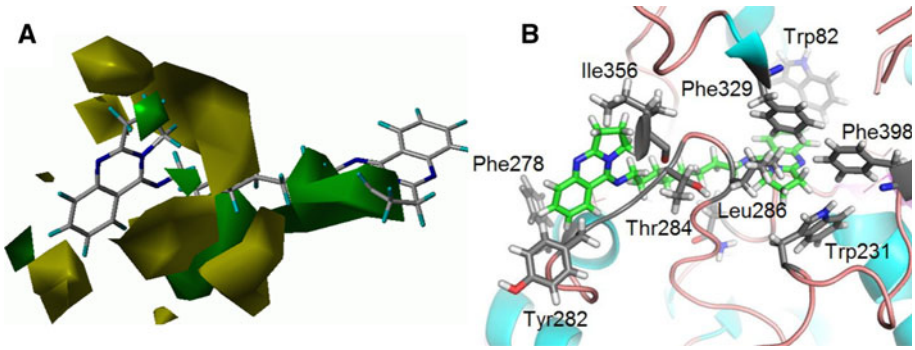

Fig. 9 **a** CoMFA-4a steric contour maps around compound **25**. *Green* isopleths enclose areas where steric interaction is favored. *Yellow* contours are areas where the steric interaction is disfavored. **b** Binding mode of Compound **25** with BChE; the carbon atoms of compound **25** are shown in *green*. The active-site residues are highlighted in *gray color*

The red contour shows favorable electronegative region and the blue contour shows the region where electropositive region is favored. These contour maps (as depicted in Figs. 8 and 9) give us some general insight into the nature of the receptor-ligand binding regions.

3.3.1 CoMFA contour maps

One of the most active compounds in the series (compound **25**) is shown superimposed with the CoMFA contour maps in Fig. 8. The different regions in this ligand series used to describe SAR are marked in Fig. 2.

A green contour is present near the alicyclic ring attached to the quinzaolinimine group in core region. This shows that bulky group is favored in this region. This is consistent with the reported experimental results. Compounds **1** and **4** have a five- to eight-membered ring in this region. Increase in ring size from Compound **1** (five-membered ring) to Compound **4** (eight-membered ring) leads to increase in the inhibitory activity. A yellow contour is adjacent to the green contour in the core region. This shows that the favorable bulky region is immediately surrounded by unfavorable steric interaction region. The yellow contour is also present at the –CH2– linker group near the core region. This shows that bulky groups like phenyl ring directly attached to the imine nitrogen will have unfavorable steric interaction. This explains the difference in the activity for compounds **1** and **9**. Compound **9** has a phenyl ring with ethyl linker which places it away from the unfavorable yellow contour region and has better activity than Compound **1**. The yellow contour is present near the #7-position of the quinazolinimine group (core region). This shows that either –Cl or $–CH_3$ is the optimal groups at this position. Introducing more bulky groups at this position will result in steric clash. Green contour is present in both the linker region and the peripheral group. The phenyl ring of compounds **9**–**12** is present near the green contour in the linker region. This explains the increased activity for these compounds when compared with compounds **1**–**4**. The peripheral quinazolinime group is also present in the green contour which shows that steric groups are favored in peripheral region. The peripheral quinazolinimine group is surrounded by yellow contour which shows that further bulky substitutions are not favored in this region. The quinazolinimine group in the peripheral region in compounds **19**–**28** is present in the green contour region. This is consistent with experimental activity. In comparison with non-homobivalent ligands (for example, Compounds **4**, **12**, **17,** and **32**), there is

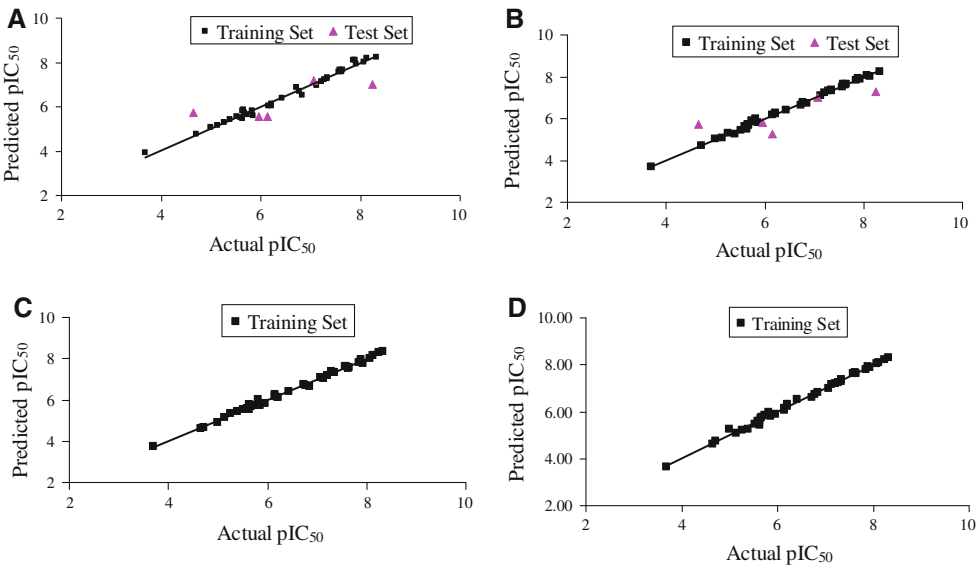

Fig. 10 Plots of the predicted pIC_{50} values versus the actual pIC_{50} values. **a** CoMFA-3a model using the training set of 37 compounds; **b** CoMSIA-3b model using the training set of 37 compounds; **c** CoMFA-4a model using the training set of 42 compounds; and **d** CoMSIA-4b model using the training set of 42 compounds

considerable increase in activity in case of homobivalent ligands (Compounds **19** and **28**). The red contour region (favorable electronegative group) is found near the terminal imine (=N–CH_2–) nitrogen at the peripheral region. This shows that electronegative group at this region is favored. Blue contour region shows that electropositive groups are favored in this region. The free amino group of compound **34** is present near this region.

We also developed receptor-based CoMFA models. The CoMFA-3a model developed with the docked poses using a training set of 37 compounds has a q^2 value of 0.579 and r^2 value of 0.987. The validity of the model was tested with the external test set of five compounds. CoMFA-3a model gives satisfactory activity (pIC_{50}) predictions for both the training- and test sets. The predicted activity of the compounds and their residuals are provided as supporting information and the plots obtained are depicted in Fig. 10a. The deviations of the predicted pIC_{50} values for all the compounds are less than 1.3 log unit. The final CoMFA model was developed using the entire 42 compounds as the training set. Figure 9 and Figure S9 in supporting information show the receptor-based CoMFA contour plots around compound **25**. Green contour represents favorable steric interaction and is present near the alicyclic ring in the core region. This is in agreement with the corresponding protein–ligand binding structure obtained from molecular docking/MD simulation. Based on the docked binding mode, we can see that the green contour is present near the Leu286 residue. This shows that we can explore this region with hydrophobic groups to increase the activity of compounds in this series. The green contour is also present in the linker region. Our binding mode shows that this corresponds to the interaction between the linker region and the side chain methyl group of Thr120, the side chain –$(CH_2)_2$– group of Gln119. Another green contour is present in the peripheral region. Ile356 presents near this region will have a favorable interaction with substituents in this region. Yellow contour represents the unfavorable steric interaction and is present around the linker region. This is in agreement with the binding mode as the linker region is present in the deep cavity. The yellow region corresponds to residues around the cavity and substituents in this region will have a steric clash with active-site residues. Yellow contour is also present around the peripheral group. This is in agreement with the active site. This shows that while hydrophobic groups are favored in this region, extending such groups will have a steric clash with the backbone of residues in this region. The blue contour represents region where electropositive groups are favored. Red contour represents the favorable electronegative group and is present in the linker region. Electronegative group present in this region will have a favorable interaction with Asn289 side chain. Thus, the contour map from our model correlates well with the observed active-site residues of BChE binding with the inhibitors.

3.3.2 CoMSIA contour maps

Figure S7 in supporting information shows compound **25** superimposed on the CoMSIA steric, electrostatic, hydrogen bond donor, and hydrogen bond acceptor contour plot. Overall, the CoMSIA steric and electrostatic contour maps were similar to the ones obtained from the CoMFA model. We also developed receptor-based CoMSIA models. The CoMSIA model developed with the docked poses using a training set of 37 compounds has a q^2 value of 0.551 and r^2 value of 0.996. The model was validated with the external test set of five compounds. CoMSIA-3b model gives

satisfactory activity (pIC_{50}) predictions for both the training- and test sets. The predicted activity of the compounds and their residuals are provided as supporting information and the plots obtained were depicted in Fig. 10. The deviations of the predicted pIC_{50} values for all the compounds are less than 1 log unit except for one compound. The final CoMSIA model (CoMSIA-4b) was developed using all of the 42 compounds as the training set. Figure S10 in supporting information shows the receptor-based CoMSIA contour plots around compound **25**. As seen in Figure S10, the green contours in the linker region and in peripheral region are similar to that obtained in CoMFA. Additional details of the CoMSIA contour maps are given in the supporting information.

4 Conclusion

The binding mode of a new series of BChE inhibitors were analyzed using molecular docking, molecular dynamics (MD) simulation, and 3D-QSAR analysis. The combined molecular docking, MD simulation, and 3D-QSAR modeling studies have resulted in valuable insights into BChE binding with 42 inhibitors and their structure–activity correlation. Molecular docking and MD simulations revealed the detailed structures of BChE binding with the inhibitors, demonstrating that all of these inhibitors bind with BChE in a same binding mode. Based on the determined BChE-inhibitor binding modes, we have developed receptor-based 3D-QSAR models. Further ligand-based 3D-QSAR modeling has lead to the development of two types of satisfactory 3D-QSAR models, including the CoMFA model ($r^2 = 0.974$; $q^2 = 0.732$) and the CoMSIA model ($r^2 = 0.973$; $q^2 = 0.75$), for predicting the biological activity of compounds. The interactions identified from the CoMFA and CoMSIA 3D-contour maps correlate well with the specific interactions between the inhibitors and the amino acid residues identified in the docked binding structures. The models have good predictive ability and are capable of predicting the activity of test molecules.

The insights obtained from the combined molecular docking, MD simulation, and 3D-QSAR modeling studies are expected to be valuable for future rational drug design of new BChE inhibitors. To design new quinazolinimine derivatives as more potent inhibitors of BChE, one may first construct a combinatorial library of possible virtual compounds having the common quinazolinimine scaffold with various substituents. Then, one may perform either structure-based modeling (starting from molecular docking) or ligand-based evaluation (using the CoMFA or CoMSIA model) on each compound in the virtual library. For example, the ligand-based evaluation using the CoMFA or CoMSIA model, one may employ the CoMFA or CoMSIA model to predict the IC_{50} value for each new compound, and the new compounds that are predicted to have the lower IC_{50} values will be recommended for chemical synthesis and the activity assays.

Acknowledgments The research was supported by NIH (grant R01 DA013930 to CGZ). CSR worked in CGZ's laboratory as a NIDA Summer Research Fellow (from School of Informatics, Indiana University) through a supplemental award (R01 DA013930-06S2 to CGZ). The authors also acknowledge the Center for Computational Sciences (CCS) at University of Kentucky for supercomputing time on IBM X-series Cluster with 340 nodes or 1,360 processors.

References

1. Carreiras MC, Marco JL (2004) Curr Pharm Des 10:3167–3175
2. Campiani G, Fattorusso C, Butini S, Gaeta A, Agnusdei M, Gemma S, Persico M, Catalanotti B, Savini L, Nacci V, Novellino E, Holloway HW, Greig NH, Belinskaya T, Fedorko JM, Saxena A (2005) J Med Chem 48:1919–1929
3. Salloway S, Mintzer J, Weiner MF, Cummings JL (2008) Alzheimers Dement 4:65–79
4. Rosini M, Andrisano V, Bartolini M, Bolognesi ML, Hrelia P, Minarini A, Tarozzi A, Melchiorre C (2005) J Med Chem 48:360–363
5. Schliebs R, Arendt T (2006) J Neural Transm 113:1625–1644
6. Decker M (2005) Eur J Med Chem 40:305–313
7. Zaheer-ul H, Uddin R, Yuan H, Petukhov PA, Choudhary MI, Madura JD (2008) J Chem Inf Model 48:1092–1103
8. Pan L, Tan J-H, Hou J-Q, Huang S-L, Gu L-Q, Huang Z-S (2008) Bioorg Med Chem Lett 18:3790–3793
9. Fang L, Kraus B, Lehmann J, Heilmann J, Zhang Y, Decker M (2008) Bioorg Med Chem Lett 18:2905–2909
10. Zheng F, Zhan C-G (2008) J Comput Aided Mol Des 22:661–671
11. Zhan C-G, Zheng F, Landry DW (2003) J Am Chem Soc 125:2462–2474
12. Gorelick DA (1997) Drug Alcohol Depend 48:159–165
13. Yu Q-S, Holloway HW, Utsuki T, Brossi A, Greig NH (1999) J Med Chem 42:1855–1861
14. Mesulam M-M, Guillozet A, Shaw P, Levey A, Duysen EG, Lockridge O (2002) Neuroscience 110:627–639
15. Greig NH, Utsuki DK, Ingram DK, Wang Y, Pepeu G, Scali C, Yu Q-S, Mamczarz J, Holloway HW, Giordano T, Chen D, Furukawa K, Sambamurti K, Brossi A, Lahiri DK (2005) Proc Natl Acad Sci USA 102:17213–17218
16. Duysen EG, Li B, Darvesh S, Lockridge O (2007) Toxicology 233:60–69
17. Li B, Stribley JA, Ticu A, Xie W, Schopfer LM, Hammond P, Brimijoin S, Hinrichs SH, Lockridge O (2000) J Neurochem 75:1320–1331
18. Decker M, Krauth F, Lehmann J (2006) Bioorg Med Chem 14:1966–1977
19. Decker M (2006) J Med Chem 49:5411–5413
20. Decker M, Kraus B, Heilmann J (2008) Bioorg Med Chem 16:4252–4261
21. Jorgensen WL (2009) Acc Chem Res 42:724–733
22. Joseph-McCarthy D (1999) Pharmacol Therap 84:179–191
23. Davis AM, Teague SJ, Kleywegt GJ (2003) Angew Chem Int Ed 42:2718–2736
24. Martin YC (1998) Perspec Drug Discov Design 12:3–23
25. Cramer RD, Patterson DE, Bunce JDJ (1988) Am Chem Soc 110:5959–5967

26. Kubinyi H (ed) (1993) 3D-QSAR in drug design. Theory, methods and applications. ESCOM, Leiden (NL)
27. Klebe G, Abraham U, Mietzner T (1994) J Med Chem 37:4130–4146
28. Bohm M, Sturzebecher J, Klebe G (1999) J Med Chem 42:458–477
29. AbdulHameed MDM, Hamza A, Liu J, Huang X, Zhan C-GJ (2008) Chem Inf Mod 48:179–185
30. Kuo CL, Assefa H, Kamath S, Brzozowski Z, Slawinski J, Saczewski F, Buolamwini JK, Neamati N (2004) J Med Chem 47:385–399
31. Yang G-F, Lu H-T, Xiong Y, Zhan C-G (2006) Bioorg Med Chem 14:1462–1473
32. Debnath AK (2001) Mini Rev Med Chem 1:187–195
33. Abdulhameed MDM, Hamza A, Liu J, Zhan C-GJ (2008) Chem Inf Model 48:1760–1772
34. Besler BH, Merz KM Jr, Kollman PA (1990) J Comp Chem 11:431–439
35. Singh UC, Kollman PA (1984) J Comp Chem 5:129–145
36. Rarey M, Kramer B, Lengauer T, Kleb G (1996) J Mol Biol 261:470–489
37. Rarey M, Wefing S, Lengauer T (1996) J Comput Aided Mol Design 10:41–54
38. AbdulHameed MDM, Hamza A, Zhan C-G (2006) J Phys Chem B 110:26365–26374
39. Case DA, Darden TA, III Cheatham TE, Simmerling CL, Wang J, Duke RE, Luo R, Merz KM, Wang B, Pearlman DA, Crowley M, Brozell S, Tsui V, Gohlke H, Mongan J, Hornak V, Cui G, Beroza P, Schafmeister C, Caldwell JW, Ross WS, Kollman PA (2004) AMBER 8. University of California, San Francisco
40. Jorgensen WL, Chandrasekhar J, Madura JD, Klein MLJ (1983) J Chem Phys 79:926–935
41. Berendsen HC, Postma JPM, van Gunsteren WF, DiNola A, Haak JR (1984) J Chem Phys 81:3684–3690
42. Ryckaert JP, Ciccotti G, Berendsen HC (1977) J Comput Phys 23:327–341
43. Essmann U, Perera L, Berkowitz ML, Darden TA, Lee H, Pedersen LG (1995) J Chem Phys 103:8577–8593
44. Datar P, Desai P, Coutinho E, Iyer K (2002) J Mol Model 8:290–301
45. Bush BL, Nachbar RB (1993) J Comp Aided Mol Design 7:587–619
46. Tripos Associates, Inc., 1699 S. Hanley, St.Louis MI 63144, USA
47. Nicolet Y, Lockridge O, Masson P, Fontecilla-Camps JC, Nachon F (2003) J Biol Chem 278:41141–41147
48. Sperandiodasilva GM, Sant'Anna CMR, Barreiro EJ (2004) Bioorg Med Chem 12:3159–3166